Broadband Calculable Coaxial Resistors

Marco Agustoni, *Member, IEEE*, Sophie De Préville, and Frédéric Overney, *Member, IEEE*

***Abstract*— This article describes a method to model the impedance of a Haddad-type resistor over a frequency interval ranging from 10 to 200 MHz, hereafter defined as low frequency–radio frequency (LF–RF) range. To this end, novel resistor standards, of 1 kΩ and 100 Ω, have been designed and manufactured with the aim of sharply identifying the nodes that define the impedance. Resistor modeling is divided into two main parts: the first one, describing the central coaxial core and the second part, describing the connectors through physical simulations and a subsequent analytical approach. The results show a remarkable good agreement between measured and modeled impedance over the whole considered frequency range. Uncertainty values allow for the traceability of the resistors up to high frequencies and for the calibration of commercial impedance analyzers within the LF–RF range.**

***Index Terms*— Frequency gap, Haddad resistor standard, impedance comparison, impedance modeling, physical simulations.**

I. Introduction

OVER the years, National Metrology Institutes (NMIs) have developed refined techniques to realize the impedance for the low frequencies (LFs) [1], which roughly range up to several kHz, as well as for the radio frequency (RF) range [2]. Such techniques are based on two distinct measurement methodologies, each exploiting to its advantage the physical laws deriving from frequency values in the considered range to determine the impedance. In the LF range, the impedance is basically defined as the complex ratio between the voltage applied at two terminals of the measured element and the current flowing through it. The definition of the impedance for RF is instead related to the scattering of an incident electromagnetic (EM) wave on a specific surface (e.g., coaxial port) of the measured element. In this context, the transformer-based coaxial bridge allows to perform impedance measurements with a relative accuracy below the $\mu\Omega/\Omega$ level for the LF range, whereas the RF range is well covered by the vector network analyzer (VNA), whose accuracy is rather of order of percent fraction.

Finding a method that guarantees traceability of impedance for the gap that can be defined between the LF and RF ranges is still an open issue in electrical metrology. In the past, different approaches have been developed with the aim of reducing the uncertainty of impedance measurements in this challenging frequency range [3], [4]. In particular, some methods attempt to extend the LF limit of the calculable impedance standards [5], [6], [7], [8], [9], [10]. Other techniques aim to reduce the frequency gap by improving the accuracy from the RF side [11], [12], or by determining, through resonant frequencies measured with VNA, the elements of the equivalent circuit associated with the impedance standards [13], [14], [15], [16].

In a previous article [17], we have presented two different modeling methods, respectively based on physical simulations and resolution of differential equations, to realize the impedance within the LF–RF range, whose limits were fixed at 1 and 100 MHz. In both approaches, the resulting impedance was assumed to be continuous along this interval and the values at the border matched the high accuracy measurements that can be performed for high- and LF ranges. In this context, the accuracy level for the LF–RF impedance realized with a Haddad-type resistor [18] covers a range from 6 ppm to 7%. The noticeable increment of the uncertainty value in the high-frequency range is attributable to the fact that the resistor was originally designed to work at LFs. This is mainly due to the difficulty of reproducing with an analytical model the geometric structure of its connective part, where the coarse soldering points prevented to accurately determine their intersection with the inner conductor.

In this article, we propose a novel architecture for resistor standard belonging to the Haddad typology, which can be flexibly described by a simple analytical model. Measurements have been performed with four standards each having the impedance value of 100 Ω and 1 kΩ, respectively. The new standards have been entirely designed and manufactured at the Swiss Federal Institute of Metrology (METAS). The geometry of these resistors provides improvements especially in the area dedicated to the connectors, allowing for locating with a considerably better resolution than their previous versions, the nodes defining the impedance.

A finite element analysis, performed with COMSOL® multiphysics simulation software [19], shows how the Haddad resistors can be modeled with great precision by decoupling the connectors from the central coaxial line. An analytical model describing the totality of the resistor (i.e., central and connective part together) with associated uncertainty values can finally be developed on the basis of the well-known transmission line equations (TLEs). With this approach, it is possible to guarantee the traceability of the 1 kΩ and 100 Ω resistor standards up to 200 MHz with an uncertainty of 0.4% and 2.4%, respectively. Taking these results into consideration, therefore, it is possible to set up a calibration system for some commercial impedance analyzers that work on a frequency band ranging from a few tens to a few hundred MHz.

Manuscript received 4 January 2023; revised 14 February 2023; accepted 13 March 2023. Date of publication 3 April 2023; date of current version 14 April 2023. The Associate Editor coordinating the review process was Dr. Isaac Fan. *(Corresponding author: Marco Agustoni.)*

The authors are with the Federal Institute of Metrology METAS, 3003 Bern-Wabern, Switzerland (e-mail: marco.agustoni@metas.ch).

Digital Object Identifier 10.1109/TIM.2023.3264021

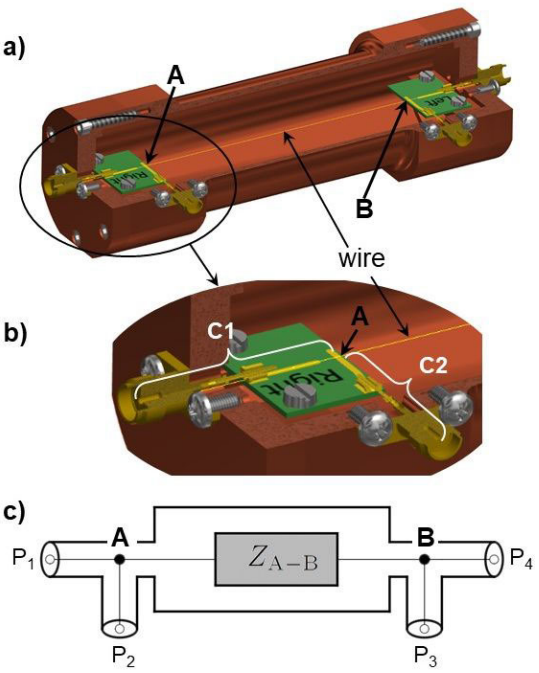

Fig. 1. Design of the 4TP resistor standard: (a) biplanar 3-D drawing cutting; (b) enlargement of the connectors area showing the connector types C1 and C2; and (c) schematic representation showing the impedance of interest between nodes A and B.

The article is organized as follows. In Section II, we present the design of the resistor standards. Section III gives some details about their measurements with the VNA. The impedance model is described in Section IV, whereas the uncertainty budget is computed in Section V. Finally, Section VI provides some closing remarks and outlines the future stages of the research activity.

II. Design of the Resistor Standard

In this section, a new design for Haddad resistor standards is presented. What differentiates them from the previously used version [17], which were made for working within the kHz frequency range, is mainly a more refined structure at the points where the connective parts cross the coaxial inner conductor. This simple solution allows to sharply realize the impedance also for frequencies up to few hundreds of MHz, as explained in more detail in the following.

As can be seen from the picture in Fig. 1(a), these resistor types are characterized by a relatively simple geometry. The central part (between the nodes A and B) forms basically a coaxial line in which a resistive central wire (of radius r_w) acts as an inner conductor, while the outer metal tube (inner radius r_i and outer radius r_o) serves as an outer conductor. At either end of the coaxial part, there are two connector blocks each made up of two connector types hereafter referred to as C1 and C2. The two connectors C1 are axially aligned with the resistive wire, while the two connectors C2 are arranged orthogonally to the wire's axis.

As shown in the enlargement of the connectors block in Fig. 1(b), both C1 and C2 are composed of two principal parts. The first one, common to both connector types, is formed by the subminiature version A (SMA) coaxial connector, which provides the connection of the resistor with the external world. The second part, instead, ensures the electrical contact between the SMA connector and the node A (respectively B) where the resistive wire is soldered on. It consists in a cylindrical rod, inserted between the SMA inner conductor, and a support lying on a printed circuit board (PCB) track. In this part of the circuit, however, the two connector types present an asymmetry. While for C2 the node A (respectively B) is situated at the end of the PCB track, for C1 this is connected with its PCB track through a short piece of resistive wire. This way of joining wire and connectors leads to a sharp definition of the impedance because the contact resistance between wire and connectors is part of the connector's resistance self and not part of the impedance Z_{A-B}.

TABLE I
Geometrical and Material Parameters of the Haddad-Type Resistors

parameter	symbol	value		uncertainty	unit
		100 Ω	1 kΩ		
wire length	ℓ_{A-B}	87.1	237.5	1	mm
wire radius	r_w	11.5	10	1	μm
tube's inner radius	r_i	15		0.2	mm
tube's outer radius	r_o	17		0.2	mm
wire el. conductivity	σ_1	2.11	0.744	0.05	MS/m
air el. conductivity	σ_2	$5{\cdot}10^{-6}$		$1{\cdot}10^{-6}$	nS/m
tube el. conductivity	σ_3	59.6		5	MS/m

Since both connector blocks have been designed to be identical and symmetric, we can define C1 and C2 to be the connector types associated with the ports P_1, respectively P_2 connected to node A and, symmetrically, to the ports P_4, respectively P_3 connected to the node B. In the modeling of the standard described in Section IV, such symmetries are taken into account.

The impedance measurements presented in this article have been performed on four resistors manufactured for this purpose at METAS. Two of these have a nominal impedance value of 100 Ω, while the other two have a nominal value of 1 kΩ. The only difference between the two sets of resistors is represented by the length ℓ_{A-B}, the radius and the material of the resistive wire (costantan and evanhom, respectively), while the outer shielding is made of a copper tube for all four resistors. Geometrical and material parameters, with corresponding uncertainty, of the Haddad resistors are summarized in Table I.

Fig. 1(c) illustrates a schematic representation of the four-terminal pair (4TP) resistor. The impedance of such standard, defined between nodes A and B, can be obtained by applying the four terminal-pair definition [20] widely used in impedance metrology. To this end, the resistor ports are associated with the following labels: HC, LC, HP, and LP identifying the procedure, whereby current and voltage, respectively, are set or measured. At one side of the resistor, a current is injected into one port, labeled HC, while a voltage is measured at the other port, indicated with HP, by keeping the current equal to 0. On the other side of the resistor, the output current is measured at one port, labeled LC, whereas to the other port, indicated with LP, current and voltage are

TABLE II
PORT CONFIGURATIONS DEFINING FOUR TERMINAL-PAIR MEASUREMENTS

	Configuration #							
port	1	2	3	4	5	6	7	8
P_1	HP	HP					LC	LC
P_2			HP	HP	LC	LC		
P_3	LC		LC			HP		HP
P_4		LC		LC	HP		HP	

set to 0. Finally, the impedance can be computed as a ratio between voltage V measured at HP and current I, measured at LC as follows:

$$Z_{4TP} = \left.\frac{V_{HP}}{I_{LC}}\right|_{\substack{I_{LP}=0, V_{LP}=0 \\ I_{HP}=0.}}. \quad (1)$$

While in LF range (typically below few kHz), the value of the four terminal-pair impedance barely depends on the choice of the connectors used to measure the voltage V and current I, the situation is different at higher frequency (above 100 MHz) because the effect of the connectors on the four terminal pair impedance becomes significant. In this case, the choice of the connectors becomes critical.

Table II lists all the combinations whereby HP and LC can be configured over the four resistor ports. By definition, the configurations k and $9-k$ (for $k = 1$ to 4) are equivalent. Moreover, due to the fact that ports P_1 and P_4, and the ports P_2 and P_3, present the same connector type, namely C1 and respectively C2, the configurations 1 and 4 are also equivalent. Therefore, over the eight configurations presented in Table II, only three configurations lead to distinct 4TP impedance values at high frequencies, namely $Z^{\#1}_{4TP}$, $Z^{\#2}_{4TP}$, and $Z^{\#3}_{4TP}$. At LF, the values of the three different impedances converge to the same dc resistance.

III. VNA MEASUREMENTS

The new Haddad resistor standards have been measured, for frequencies ranging from 9 kHz to 3 GHz, with a commercial four-port VNA from Keysight, model ENA E5080A. The open/short/load calibration procedure has been performed before measurements and uncertainty calculation has been applied according to [2] using dedicated software VNA tools. The picture in Fig. 2 illustrates the measurement setup used for the VNA measurements of the four terminal-pair standard. For each frequency, the instrument returns a scattering parameter matrix $\mathbf{S}$ which fully characterizes the electrical behavior of the multiport device. The components S_{ij} of such a matrix, which in the case of a four-port standard has 4×4 size, are the results of the complex ratio b_i/a_j, where a_j is the incident wave at the port j and b_i is the reflected wave at the port i.

Once the scattering matrix $\mathbf{S}$ is obtained through VNA measurements, the 4TP impedance for the configuration #1 can be computed according (1) as follows:

$$Z^{\#1}_{4TP} = \frac{Z_{21}Z_{34}}{Z_{31}} - Z_{24}. \quad (2)$$

The terms Z_{ij}, which are the results of the ratio between voltages V measured at the port i and currents I measured at the port j, represent the elements of the impedance matrix $\mathbf{Z}$ derived from the result of the following relation [3]:

$$\mathbf{Z} = \left(\mathbb{1} - \mathbf{S}\right)^{-1} \cdot \left(\mathbb{1} + \mathbf{S}\right) \cdot Z_r. \quad (3)$$

In this case, $\mathbb{1}$ denotes the 4×4 identity matrix, and Z_r the 50 Ω reference impedance. Similarly, the 4TP impedance for the configurations #2 and #3 can also be obtained from other element combinations of the $\mathbf{Z}$ matrix.

Fig. 3 shows the modulus of the 4TP impedance as a function of frequency f calculated according to configurations #2 and #3 from data coming from the measurements of a 1 kΩ resistor with the VNA. The different frequency-dependent behavior of measured data by adopting two different configurations immediately becomes apparent. While at LF the values coincide, a clear disagreement begins to be noticeable starting from 200 MHz. This clearly demonstrates an asymmetry

Fig. 2. Measurement setup used for the VNA measurements.

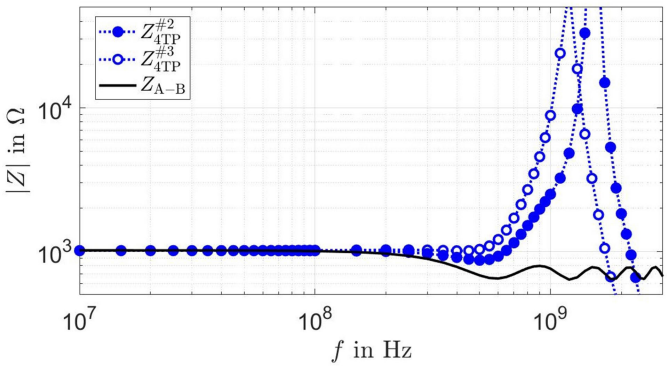

Fig. 3. Impedance modulus $|Z|$ versus frequency f (in log–log scale) of a 1 kΩ resistor calculated, according to configuration #2 (solid symbols with dotted line) and #3 (open symbols with dotted line), from values measured of the four-port standard with the VNA. The calculated impedance Z_{A-B} (solid line) is also represented.

between the connector types C1 and C2 and their fundamental influence on the 4TP impedance definition.

The frequency dependence of the impedance calculated between nodes A and B according the approach described in [18] is also represented in Fig. 3. This curve remarkably shows the fundamental effect that connectors have for an accurate computation of the 4TP impedance in the high frequency range.

IV. Modeling the Standard Resistor

The results of the measurements performed with the VNA shown in Section III prove that, if we want to correctly describe the proposed broadband resistor standards, we need to accurately model the connective parts. To this end, in this section, we present an approach divided in two steps. The first step, described in Section IV-A, covers the resolution of the TLE between the nodes A and B, in the central coaxial part of the resistor, to determine the impedance $Z_{\text{A–B}}$. Second, we assess the effect of the connectors with the aim of correcting $Z_{\text{A–B}}$ and to finally obtain the 4TP impedance Z_{4TP}.

In this regard, a numerical model based on the finite elements simulation of the entire connector block (described in Section IV-B) provides the consistency of the impedance in the LF–RF range. Moreover, it confirms that the discrepancy between measured Z_{4TP} and calculated $Z_{\text{A–B}}$ is due to the connector effects and not to a miscomputation of $Z_{\text{A–B}}$. In the analytical model proposed in Section IV-C we estimate the fundamental circuit parameters characteristics of the connector block. In this way, we are finally able to model the impedance of the resistor, within the calculated uncertainty values, as a function of frequency along the LF–RF range.

A. Coaxial Line Model

The central part of the Haddad resistor standard can be considered as a two-port linear network [21], which relates voltages and currents between the points A and B. Mathematically, this is represented by the following linear system:

$$\begin{pmatrix} V_A \\ I_A \end{pmatrix} = \mathbf{M}_{\text{A–B}} \cdot \begin{pmatrix} V_B \\ I_B \end{pmatrix} \tag{4}$$

where $\mathbf{M}_{\text{A–B}}$ is a 2×2 matrix, whose components are the so-called *ABCD* parameters [22]. The geometry of the central part is characterized by a pure cylindrical symmetry defined by its central conductor, the evanohm wire tightened between points A and B, surrounded by the outer metal shield. Ideally, this represents a homogeneous, infinite coaxial line and the elements of the impedance matrix $\mathbf{M}_{\text{A–B}}$ can be computed by solving the coupled TLE as described in [17]. The components of $\mathbf{M}_{\text{A–B}}$ can be represented with the following approximation:

$$\mathbf{M}_{\text{A–B}} \approx \mathbf{M}_{\text{TLE}} = \begin{pmatrix} \cosh(\gamma \ell) & Z_0 \sinh(\gamma \ell) \\ \sinh(\gamma \ell)/Z_0 & \cosh(\gamma \ell) \end{pmatrix} \tag{5}$$

where γ and Z_0 denote the propagation constant and the characteristic impedance respectively, whereas ℓ represents the length of the coaxial line.

The two terminal-pair impedance between the points A and B, separated by a distance $\ell_{\text{A–B}}$, can be obtained by solving the linear system (4) according to the definition [20]

$$Z_{\text{A–B}} = \left. \frac{V_{\text{A}}}{I_{\text{B}}} \right|_{V_{\text{B}}=0.} = Z_0 \sinh(\gamma \ell_{\text{A–B}}). \tag{6}$$

The values of $\gamma = (z_0 \cdot y_0)^{1/2}$ and $Z_0 = (z_0/y_0)^{1/2}$ are the result of the multiplication and ratio between the impedance z and the admittance y per unit of length along the coaxial line. Such quantities, which depend on the angular frequency ω, can be determined by following the calculation procedures described in [23] and [24]. The described approaches consist in directly calculating the complex components of z and y from geometric dimensions and material properties of the resistor. For the sake of clarity, it is worth mentioning that to determine these values, some approximations are taken into account. These prove to be valid when operating with frequencies that are below the threshold given by the cutoff value f_c for the transverse EM mode [21]

$$f_c \approx \frac{1}{\pi (r_{\text{w}} + r_{\text{i}}) \sqrt{\varepsilon \mu}} \tag{7}$$

where ε and μ are the electrical and magnetic permittivity, whereas r_{w} and r_{i} are the wire and the tube's inner radius as reported in Table I. Geometrical and material parameters of the presented Haddad resistor type allow to determine the impedance between nodes A and B for a frequency limit up to about 6 GHz, which is a factor 2 greater than the maximal frequency value considered in this article.

The modulus of the impedance $Z_{\text{A–B}}$, calculated for the 1 kΩ standard, is represented in Fig. 3 as a function of the frequency. The remarkable difference between the measured and the calculated 4TP impedance above 100 MHz points out that such a simple model cannot properly describe a broadband resistor standard.

B. Numerical Model of the Connectors

In this section, we provide the description of a model obtained through physical simulations performed on the connector blocks on each side of the central coaxial part of the resistor. Material and geometry reconstructed in the finite element simulation software faithfully reproduce the assembly of the two connectors C1 and C2 plus the first portion of the wire that from point A (resp. B) faces the cylindrical coaxial part of the resistor as illustrated in the enlargement of Fig. 1(b). The resulting object represents a three-port network system.

The first two ports, corresponding to P_1 and P_2 (resp. P_4 and P_3) are the section of the SMA connectors, while the third port is formed by the section of the central coaxial line and named P_{A} (resp. P_{B}). In this context, the definition of lumped port can be adopted, as a first-order approximation, up to the highest frequency taken into account in this work, which is 3 GHz. The simulation software solves the Ampère's law equations in frequency domain all over the schematized connector block as shown in Fig. 4, where the steady-state propagation of the EM field is illustrated. As a result, simulations quantify the electrical behavior of the three-port network

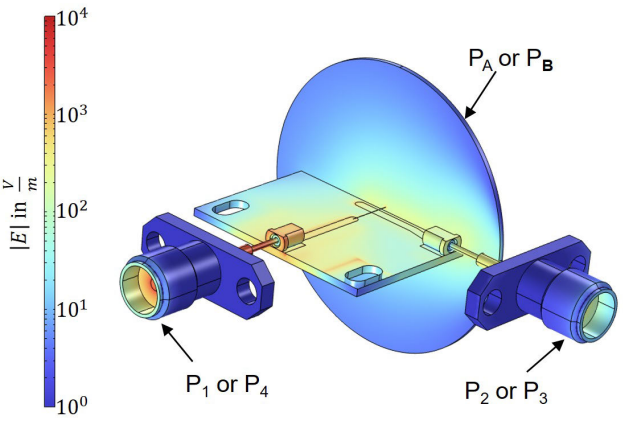

Fig. 4. Representation of the electric field norm at 1.7 GHz on the schematized connector block realized with COMSOL simulations.

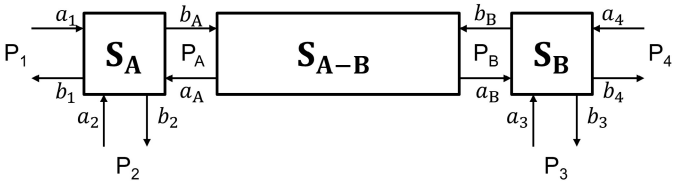

Fig. 5. Four terminal-pair standard represented with a three-two-three cascaded network system described by $\mathbf{S}_A$, $\mathbf{S}_{A-B}$, and $\mathbf{S}_B$ scattering matrices, respectively.

for each considered frequency through a scattering parameter matrix $\mathbf{S}_{3P}$.

A two-port network relating incident and reflected EM-waves in the central part of the resistor between points A and B (i.e., ports P_A and P_B) can also be described through the scattering matrix $\mathbf{S}_{A-B}$. The elements of $\mathbf{S}_{A-B}$ are determined from the calculated elements of the matrix $\mathbf{M}_{A-B}$ defined in (5) using transformation equations [25].

In general, the 4TP resistor can be described as a cascaded network system through the scattering matrices $\mathbf{S}_A$ and $\mathbf{S}_B$, associated with the three-port networks of the connector blocks and the scattering matrix, $\mathbf{S}_{A-B}$, associated with the two-port network of the central part. Such a representation is illustrated by a block diagram in Fig. 5.

By taking into account that, first, in our model the connector part in both sectors A and B are defined as identical and therefore matrices $\mathbf{S}_A$ and $\mathbf{S}_B$ are substituted by the simulation result matrix $\mathbf{S}_{3P}$, and, second, that incident waves of the two-port network correspond to reflected waves of the three-port networks and vice versa, it is possible to set up the following three linear systems that chain incident and reflected EM waves over the whole resistor:

$$\begin{cases} (b_1\ b_2\ b_A)^T = \mathbf{S}_{3P} \cdot (a_1\ a_2\ a_A)^T \\ (a_A\ a_B)^T = \mathbf{S}_{A-B} \cdot (b_A\ b_B)^T \\ (b_3\ b_4\ b_B)^T = \mathbf{S}_{3P} \cdot (a_3\ a_4\ a_B)^T. \end{cases} \tag{8}$$

From the system of equations (8), it is possible to obtain, by carrying out the algebraic steps shown in detail in the Appendix A, a scattering matrix $\mathbf{S}_{4P}$ that describes the electrical behavior of the presented four-port resistor

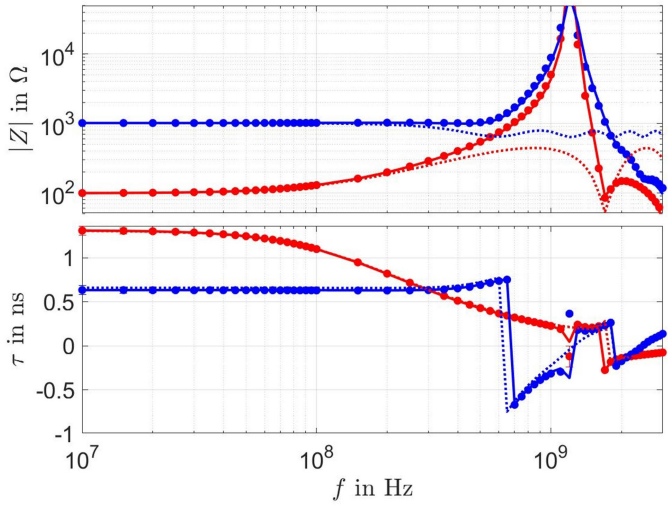

Fig. 6. Frequency dependence of impedance measured (symbols) and modeled (solid lines) according to the configuration #2 for the 100 Ω (in red) and 1 kΩ (in blue) resistor standards. Dotted lines represent Z_{A-B} as calculated in Section IV-A. Top plot: impedance modulus $|Z|$ versus frequency (log-log scale). Bottom plot: time constant τ versus frequency (log scale).

as follows:

$$(b_1\ b_2\ b_3\ b_4)^T = \mathbf{S}_{4P} \cdot (a_1\ a_2\ a_3\ a_4)^T. \tag{9}$$

The impedance matrix $\mathbf{Z}$ of the numerical model can then be calculated by substituting $\mathbf{S}_{4P}$ in (3) and, consequently, through its components it is possible to derive the 4TP impedance of the resistor standard according to the chosen configuration as shown, e.g., in (2).

In Fig. 6, the impedance measured with the VNA is compared against the impedance modeled with simulations for both the 100 Ω and the 1 kΩ standard types. A very good agreement can be noticed over the whole frequency range for the two illustrated values: the modulus $|Z|$ and the time constant $\tau = \angle Z/\omega$. This confirms two important aspects. First, the effect of the connective part has been accurately reproduced through the simulations, and second, the resistor modeling can be decomposed into two independent parts.

It is interesting to notice that the time constant obtained from the central part of the model alone (i.e. from Z_{A-B}) describes very well the measured time constant of the 4TP standard over the whole frequency range. This can be explained by the fact that the phase shift between the voltage and the current used to obtain the impedance is mainly related to the geometrical distance between the HP and LC ports. Distance that is in turn dominated by the length ℓ_{A-B} of the resistive wire rather by the length connectors C1 and C2. The effect of the connector on the time constant is therefore only a second-order effect, at least in the considered frequency range.

C. Analytical Model of the Connectors

The results presented in Section IV-B clearly prove that a broadband resistor standard can be accurately described by splitting the modeling into two simple steps: one covering the connector blocks and the other considering the central coaxial part. Based on this consideration, in this section we

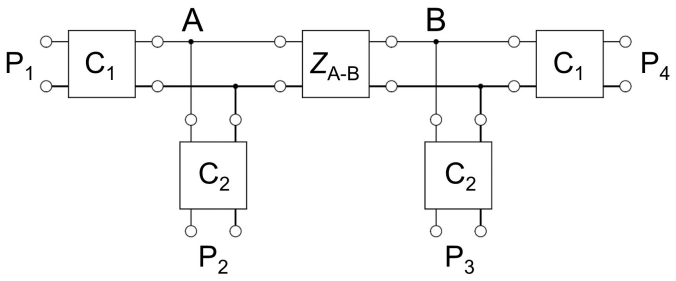

Fig. 7. Block diagram of the Haddad-type resistor standard subdivided in a series of five two-port networks system.

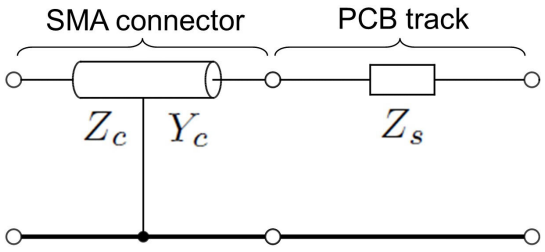

Fig. 8. Circuit diagram of connector types C1 and C2.

develop an analytical model describing both connector types, C1 and C2, in terms of the elementary parameters associated with its equivalent circuit. These parameters are then fit to the VNA data at the high-frequency range, thus providing uncertainty boundaries that confer sensitivity to our model.

To this end, the resistor standard geometry has been ideally subdivided in five circuit blocks, each one defined as a two-port network system as illustrated in Fig. 7. It can be noticed, that one of these represents the central coaxial line, whose impedance $Z_{\text{A–B}}$ has been previously determined. The remaining blocks correspond to connector types C1 and C2 that are located on each side of the coaxial part between the node A (respectively B) and the ports P_1 and P_2 (respectively P_4 and P_3). The relation between currents and voltages at the input (in) and output (out) terminals of each involved two-port network can be represented in a general form by adopting the transmission matrix formalism defined in [22]. The resulting linear system can thus be written as

$$\begin{pmatrix} V_{\text{in}} \\ I_{\text{in}} \end{pmatrix} = \mathbf{M}_{\text{2P}} \cdot \begin{pmatrix} V_{\text{out}} \\ I_{\text{out}} \end{pmatrix}, \quad \mathbf{M}_{\text{2P}} = \begin{pmatrix} A & B \\ C & D \end{pmatrix}. \tag{10}$$

By applying the 4TP definition [20] to the resistor ports and the two-port network concatenation properties, the system (10) produces the two following coupled equations:

$$V_{\text{HP}} = (A_{\text{HP}} D_{\text{HP}} - B_{\text{HP}} C_{\text{HP}}) \frac{V_{\text{A}}}{D_{\text{HP}}} \tag{11}$$

$$I_{\text{LC}} = C_{\text{LC}} V_{\text{B}} + D_{\text{LC}} I_{\text{B}} \tag{12}$$

where the $ABCD$ parameters of $\mathbf{M}_{\text{2P}}$ describe the port with measured voltage (HP) or output current (LC). The two-port networks, as previously defined, satisfy the reciprocity condition [22], which implies that the determinant of $\mathbf{M}_{\text{2P}}$ is equal to 1. For this reason, (11) simplifies further to

$$V_{\text{HP}} = \frac{V_{\text{A}}}{D_{\text{HP}}}. \tag{13}$$

According to (1), it is possible to obtain the 4TP impedance as a function of the $ABCD$ components of the involved transmission matrices by dividing (13) and (12) and by eliminating the dependence on voltages and currents at points A and B with (6). Finally, the most simplified form of 4TP impedance for this model yields

$$Z_{\text{4TP}} = \frac{Z_{\text{A–B}}}{D_{\text{HP}} D_{\text{LC}}}. \tag{14}$$

The three impedance configurations, introduced in Section II, allow to express (14) in relation to the connector types C1 and C2, according to the symmetry characteristic of the diagram illustrated in Fig. 7, as follows:

$$Z_{\text{4TP}}^{\#1} = \frac{Z_{\text{A–B}}}{D_{\text{C1}} D_{\text{C2}}} \tag{15a}$$

$$Z_{\text{4TP}}^{\#2} = \frac{Z_{\text{A–B}}}{D_{\text{C1}}^2} \tag{15b}$$

$$Z_{\text{4TP}}^{\#3} = \frac{Z_{\text{A–B}}}{D_{\text{C2}}^2}. \tag{15c}$$

The parameter D in the transmission matrix describes thus the correction due to the connector-type C1 or C2. Such correction factors can be easily determined from the VNA measurements and the calculated impedance $Z_{\text{A–B}}$, by respectively considering (15b) and (15c)

$$D_{\text{C1}} = \sqrt{\frac{Z_{\text{A–B}}}{Z_{\text{4TP}}^{\#2}}} \tag{16a}$$

$$D_{\text{C2}} = \sqrt{\frac{Z_{\text{A–B}}}{Z_{\text{4TP}}^{\#3}}}. \tag{16b}$$

The model of the connector areas is depicted in Fig. 8. The diagram points out how C1 and C2 can be described by basically dividing their structure in two main parts. The first part consists of a coaxial line, defined by the SMA connector and the coaxial portion through the outer conductor of the standard, which is described by a distributed impedance $Z_c = R_c + j\omega L_c$ and a distributed admittance $Y_c = G_c + j\omega C_c$. The remaining circuitry, consisting of the PCB track up to the point A (respectively B), is characterized by series impedance $Z_s = R_s + j\omega L_s$.

Being a chaining of two-port networks, this model can also be described by an $ABCD$ matrix relating incoming and outgoing currents as described in (10). In this case, the value of $\mathbf{M}_{\text{2P}}$ is the result of the following matrix multiplication:

$$\mathbf{M}_{\text{2P}} = \begin{pmatrix} \cosh(\gamma^c) & Z_0^c \sinh(\gamma^c) \\ \sinh(\gamma^c)/Z_0^c & \cosh(\gamma^c) \end{pmatrix} \begin{pmatrix} 1 & Z_s \\ 0 & 1 \end{pmatrix}$$

where $\gamma^c = (Z_c/Y_c)^{1/2}$ and $Z_0^c = (Z_c Y_c)^{1/2}$ are the TLE approximation components of the coaxial connector part. The D component of $\mathbf{M}_{\text{2P}}$ giving the correction factor due to the connectors has the following value:

$$D = Z_s \sinh\left(\sqrt{Z_c Y_c}\right) \sqrt{\frac{Y_c}{Z_c}} + \cosh\left(\sqrt{Z_c Y_c}\right). \tag{17}$$

TABLE III
PARAMETERS OF THE CONNECTOR'S ANALYTIC MODEL

parameter	Connector type C1	C2	unit
R_c	0.10 ± 0.50	0.10 ± 0.50	Ω
L_c	8.70 ± 0.20	6.44 ± 0.20	nH
G_c	10 ± 10	10 ± 10	nS
C_c	1.43 ± 0.10	1.06 ± 0.10	pF
R_s	10 ± 10	0.5 ± 3.0	Ω
L_s	9.28 ± 0.20	8.17 ± 0.20	nH

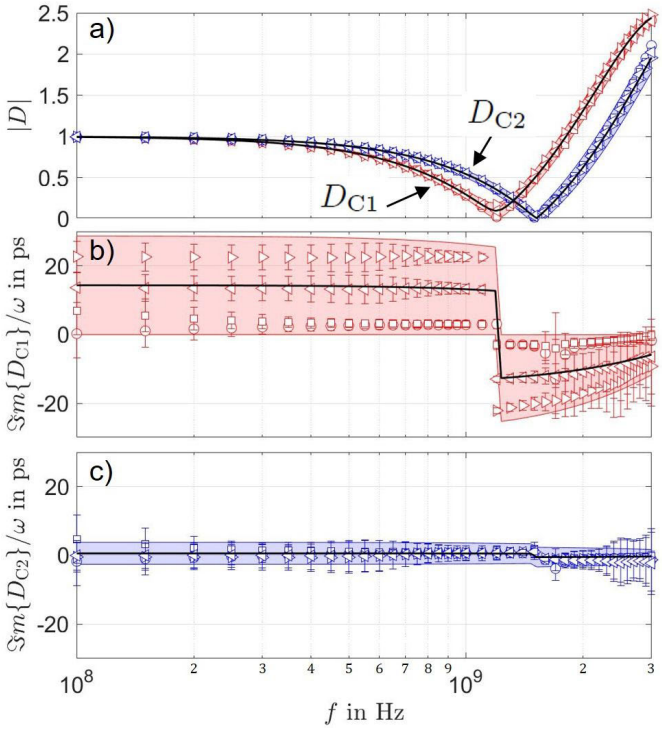

Fig. 9. Frequency dependence (in log scale) of (a) modulus of the correction factor D for both connector types C1 and C2, and of the imaginary part of D over the angular frequency ω for connector types, (b) C1, and (c) C2. Symbols represent the values obtained with VNA measurements performed on each of the four different resistor standard, whereas solid lines and shaded areas are the results, and respectively the uncertainties of the analytic model.

The values of the impedance and admittance parameters contained in (17), with corresponding uncertainty, are listed for both connector types C1 and C2 in Table III. The parameters have been adjusted to make the model (17) correctly describe the measured values obtained from (16a) and (16b) in the high-frequency range above 100 MHz, as shown in Fig. 9. The uncertainties have been determined in a conservative way; therefore, the same parameters can be used to model each of the four-resistance standard.

The most significant difference between the parameter values characterizing the connector types C1 and C2 concerns the series resistance R_s. The reason is due to the fact that a short piece of resistive wire connects the node A (respectively B) and the PCB track of C1 [see Fig. 1(b)]. Therefore, in this case, R_s is 50 times greater than for C2, which does not present this characteristic. It can also be noticed that the values of C_c and L_c for the connector type C1 are greater than those for the connector type C2, although, in this instance the difference is less significant. This can be explained by the portion of coaxial line inside the outer conductor between the SMA connector and the PCB edge. The length of this portion is indeed longer for the connector type C1 than for the connector type C2.

The comparison between the correction factor D due to connectors for values derived from the 4TP impedance measurements, as shown in (16a) and (16b), and modeled with (17) according to the parameters listed in Table III, is shown in Fig. 9. The full agreement between VNA data, measured for two 100 Ω and two 1 kΩ resistor standards, and model over the whole frequency range is noticeable. The scattering of the values inside each curve reflects mainly the homogeneity of the mechanical realization of each connector type and, to an extent reduced, the VNA measurement spread.

Fig. 9(a) shows the modulus of the correction factor D of both connector types C1 and C2. It can be seen that there is no systematic difference between the results obtained using the 100 Ω and the 1 kΩ resistance standards. For this reason, as the ratio between the size of the connector blocks and the length of the coaxial part is not the same for the two resistor types, the edge effect in the TLE analysis of the coaxial line can be considered negligible.

Fig. 9(b) and (c) represent the ratio between the imaginary part of the correction factor D and the angular frequency ω for the C1 and C2 case, respectively. The scattering of the values for the connector type C1 is significantly larger than what is obtained for the connector type C2. As previously described, this is due to a broader variation of the series resistance R_s in the connector type C1.

V. UNCERTAINTY BUDGET

In this section, we provide an estimate of the uncertainty budget for both the presented resistor standard types of 100 Ω and 1 kΩ, over the whole considered frequency range. All the computed uncertainties correspond to one standard deviation ($k = 1$). In the model proposed in Section IV, the 4TP impedance (14) is the ratio between the impedance of the central coaxial part $Z_{\mathrm{A–B}}$ (6) and the correction factor D (17) due to connectors. The uncertainty corresponding to this impedance is therefore the result of the uncertainty propagation calculated with the parameters listed in Table I, for the central coaxial part, and in Table III, for the connective part. For the sake of clarity, in the case of $Z_{\mathrm{A–B}}$, the resistance uncertainty part is calculated using these parameters only to assign the frequency dependence component, while the basis value R_{dc} comes from the calibration of the resistor standards in dc and can easily be performed with an uncertainty below 1 $\mu\Omega/\Omega$.

The main contributions of the total uncertainty estimated in the analytic model, using the UncLib library [26] developed at METAS, differ depending on the impedance value of the resistor and on the frequency range considered. In the case of the modulus of the impedance at frequencies below 500 MHz, by considering the 100 Ω Haddad, the 90% of the uncertainty is due to the resistance of the evanohm wire in the central coaxial part, while, for the 1 kΩ resistor, the

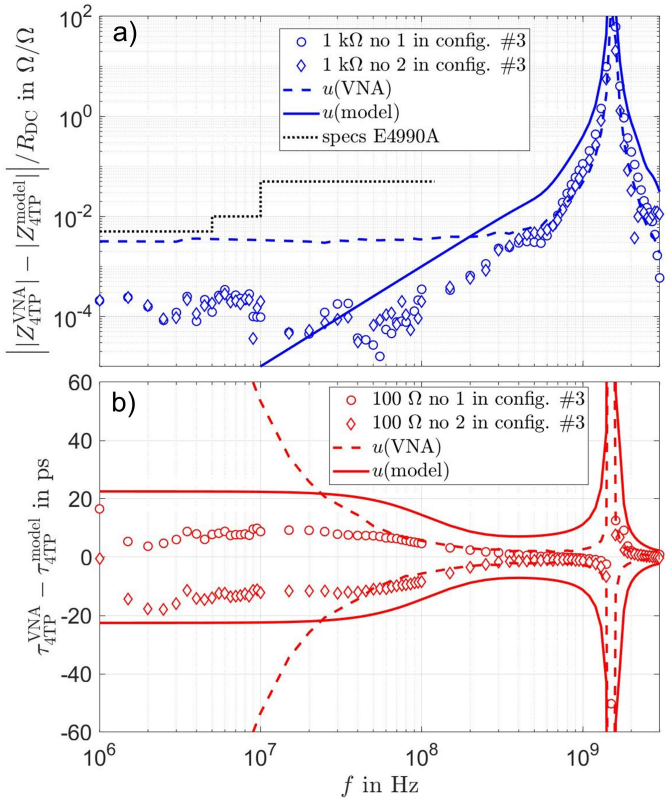

Fig. 10. Frequency dependence (in log scale) of (a) absolute relative difference (in log scale) between the modulus of measured and the modulus of modeled 4TP impedance using 1 kΩ standards (blue symbols) and (b) difference of the measured and modeled 4TP time constant using 100 Ω standards (red symbols). Dashed and solid lines represent the uncertainty limits of VNA measurements and model, respectively.

dominant contribution is provided by the connectors. The 85% of the total uncertainty is due to the capacitance C_c. Above 500 MHz, the uncertainty of both resistor types is dominated by connector contributions.

Also in the case of the uncertainty estimated for the time constant, by considering the 100 Ω resistor, the main uncertainty contribution comes from the resistance of the central evanohm wire, up to 200 MHz. For 1 kΩ Haddad instead, up to 700 MHz, the uncertainty is almost equally distributed between the resistive part of the central wire and the series resistance of the connectors R_s. Beyond these frequencies, for both types of resistors, the uncertainty is totally due to R_s.

Two examples of uncertainty analysis results are shown over the whole considered frequency range in Fig. 10(a) which illustrates the absolute relative difference between the modulus of measured and the modulus of modeled $Z_{4\ \mathrm{TP}}$ in the example of 1 kΩ standards, and in Fig. 10(b) which instead illustrates the difference of the measured and modeled 4TP time constant using the 100 Ω standards. The uncertainty of $Z_{4\mathrm{TP}}$ estimated with the analytical model is lower than the uncertainty of the VNA measurements up to 200 MHz, where it has a value of 0.4%. Beyond this frequency, where VNA is more accurate, the model is still reliable because all absolute relative differences between the modulus of the impedance of model and measurements lie within the uncertainty. This can also be observed with regard to the time constant τ. In this case the crossing with the VNA uncertainty occurs at 25 MHz and the value is about 22 ps, but then the uncertainty of the model assumes less significant values throughout the frequency range except for the resonance values.

Estimating the uncertainty of these broadband resistor standards allows for their traceability. The low values of these uncertainties down to 100–200 MHz furthermore allow for the calibration of commercial impedance analyzers. In this regard, Fig. 10 reports, as an example, the uncertainty limits claimed in the specification of the Keysight E4990A impedance analyzer up to 120 MHz, indicated with the dotted line in Fig. 10(a). It can be noticed how these are at least five times higher than the uncertainties of the presented standards.

For the sake of completeness, it is worth mentioning that, in all the measurements performed in this article and in the development of the model, the effect of the temperature on the resistance value as well as a possible short-term drift have not been taken into account. These effects concern mainly the dc resistance and not the frequency dependence and moreover, they can be considered as negligible in comparison of the other uncertainty components above 10 MHz.

VI. Conclusion

In this article, a novel design for broadband resistor standards has been presented. Improvements to the connective parts with respect their previous version [17], designed for the kHz frequency range, allow for a traceability of the new standards up to 200 MHz. A numerical model, based on physical simulations, proves that at high frequencies the contribution of connectors is crucial to properly determine the 4TP impedance of the standards at the high-frequency range. The development of a subsequent analytical model results in considerably improved impedance values through a correction factor due to the connectors, whose parameters are fit to the VNA measurement data. Such a fit allows to faithfully reproduce the data at high frequencies and, moreover, to provide the uncertainty estimation.

The results show a remarkably good agreement between measured and modeled 4TP impedance over the whole considered frequency range. The uncertainty of the proposed model is lower than the uncertainty of the VNA measured data, for both the 100 Ω and 1k Ω resistors, up to 60 MHz, respectively, 200 MHz, as regards the modulus of the 4TP impedance and up to 25 MHz, respectively, 60 MHz, as regards the time constant. The uncertainty of the modulus of the 4TP impedance has been reduced by 70 times compared with [17], by decreasing from 7% to 0.1%.

The model of the resistor standards presented in this article will allow us to set up a traceable calibration system for commercial impedance analyzers over their whole frequency range (20 Hz–120 MHz). Moreover, the accuracy obtained on the time constant of these new resistance standards will allow us to improve our present calibration measurement capabilities by at least a factor of ten [27].

Appendix A
S-Matrix Synthesis

The description of incident and reflected EM-waves for a four-terminal pair standard can be quantified through a

cascaded system of all networks defined along its circuit. Fig. 5 shows an example of a four-port resistor, which has been subdivided into a two-port network, associated with the scattering matrix $\mathbf{S}_{\mathrm{A–B}}$, and into two three-port networks, associated with scattering matrices $\mathbf{S}_{\mathrm{A}}$ and $\mathbf{S}_{\mathrm{B}}$, respectively. Mathematically, this can be expressed through the following three equations:

$$\begin{pmatrix} b_1 \\ b_2 \\ b_{\mathrm{A}} \end{pmatrix} = \mathbf{S}_{\mathrm{A}} \begin{pmatrix} a_1 \\ a_2 \\ a_{\mathrm{A}} \end{pmatrix} = \begin{pmatrix} S_{11}^{\mathrm{A}} & S_{12}^{\mathrm{A}} & S_{13}^{\mathrm{A}} \\ S_{12}^{\mathrm{A}} & S_{22}^{\mathrm{A}} & S_{23}^{\mathrm{A}} \\ S_{13}^{\mathrm{A}} & S_{23}^{\mathrm{A}} & S_{33}^{\mathrm{A}} \end{pmatrix} \begin{pmatrix} a_1 \\ a_2 \\ a_{\mathrm{A}} \end{pmatrix} \tag{18a}$$

$$\begin{pmatrix} a_{\mathrm{A}} \\ a_{\mathrm{B}} \end{pmatrix} = \mathbf{S}_{\mathrm{A–B}} \begin{pmatrix} b_{\mathrm{A}} \\ b_{\mathrm{B}} \end{pmatrix} = \begin{pmatrix} S_{11}^{\mathrm{A\text{-}B}} & S_{12}^{\mathrm{A\text{-}B}} \\ S_{12}^{\mathrm{A\text{-}B}} & S_{22}^{\mathrm{A\text{-}B}} \end{pmatrix} \begin{pmatrix} b_{\mathrm{A}} \\ b_{\mathrm{B}} \end{pmatrix} \tag{18b}$$

$$\begin{pmatrix} b_3 \\ b_4 \\ b_{\mathrm{B}} \end{pmatrix} = \mathbf{S}_{\mathrm{B}} \begin{pmatrix} a_3 \\ a_4 \\ a_{\mathrm{B}} \end{pmatrix} = \begin{pmatrix} S_{11}^{\mathrm{B}} & S_{12}^{\mathrm{B}} & S_{13}^{\mathrm{B}} \\ S_{12}^{\mathrm{B}} & S_{22}^{\mathrm{B}} & S_{23}^{\mathrm{B}} \\ S_{13}^{\mathrm{B}} & S_{23}^{\mathrm{B}} & S_{33}^{\mathrm{B}} \end{pmatrix} \begin{pmatrix} a_3 \\ a_4 \\ a_{\mathrm{B}} \end{pmatrix}. \tag{18c}$$

By carrying out the multiplication between matrices and vectors, (18a), (18b), and (18c) can be displayed through the following linear system:

$$\begin{cases} b_1 = S_{11}^{\mathrm{A}} a_1 + S_{12}^{\mathrm{A}} a_2 + S_{13}^{\mathrm{A}} a_{\mathrm{A}} \\ b_2 = S_{12}^{\mathrm{A}} a_1 + S_{22}^{\mathrm{A}} a_2 + S_{23}^{\mathrm{A}} a_{\mathrm{A}} \\ b_{\mathrm{A}} = S_{13}^{\mathrm{A}} a_1 + S_{23}^{\mathrm{A}} a_2 + S_{33}^{\mathrm{A}} a_{\mathrm{A}} \\ a_{\mathrm{A}} = S_{11}^{\mathrm{A\text{-}B}} b_{\mathrm{A}} + S_{12}^{\mathrm{A\text{-}B}} b_{\mathrm{B}} \\ a_{\mathrm{B}} = S_{12}^{\mathrm{A\text{-}B}} b_{\mathrm{A}} + S_{22}^{\mathrm{A\text{-}B}} b_{\mathrm{B}} \\ b_3 = S_{11}^{\mathrm{B}} a_3 + S_{12}^{\mathrm{B}} a_4 + S_{13}^{\mathrm{B}} a_{\mathrm{B}} \\ b_4 = S_{12}^{\mathrm{B}} a_3 + S_{22}^{\mathrm{B}} a_4 + S_{23}^{\mathrm{B}} a_{\mathrm{B}} \\ b_{\mathrm{B}} = S_{13}^{\mathrm{B}} a_3 + S_{23}^{\mathrm{B}} a_4 + S_{33}^{\mathrm{B}} a_{\mathrm{B}}. \end{cases} \tag{19}$$

By combining the equations on lines 3, 4, 5, and 8 of (19) it is possible to express a_{A} and a_{B} independently of b_{A} and b_{B}. These two terms can then be inserted in lines 1, 2, 6, and 7 to formulate the relation between the reflected and incident EM waves at the four ports of the standard resistor through the scattering matrix $\mathbf{S}$

$$\begin{pmatrix} b_1 \\ b_2 \\ b_3 \\ b_4 \end{pmatrix} = \begin{pmatrix} S_{11} & S_{12} & S_{13} & S_{14} \\ S_{21} & S_{22} & S_{23} & S_{24} \\ S_{31} & S_{32} & S_{33} & S_{34} \\ S_{41} & S_{42} & S_{43} & S_{44} \end{pmatrix} \begin{pmatrix} a_1 \\ a_2 \\ a_3 \\ a_4 \end{pmatrix} \tag{20}$$

whose matrix elements are expressed as a function of $\mathbf{S}_{\mathrm{A}}$, $\mathbf{S}_{\mathrm{A–B}}$, and $\mathbf{S}_{\mathrm{B}}$ components as follows:

$$\begin{aligned} S_{11} &= S_{11}^{\mathrm{A}} + S_{13}^{\mathrm{A}} S_{31}^{\mathrm{A}} \alpha \quad S_{12} = S_{12}^{\mathrm{A}} + S_{13}^{\mathrm{A}} S_{32}^{\mathrm{A}} \alpha \\ S_{13} &= S_{13}^{\mathrm{A}} S_{31}^{\mathrm{B}} \beta \quad S_{14} = S_{13}^{\mathrm{A}} S_{32}^{\mathrm{B}} \beta \\ S_{21} &= S_{21}^{\mathrm{A}} + S_{23}^{\mathrm{A}} S_{31}^{\mathrm{A}} \alpha \quad S_{22} = S_{22}^{\mathrm{A}} + S_{23}^{\mathrm{A}} S_{32}^{\mathrm{A}} \alpha \\ S_{23} &= S_{23}^{\mathrm{A}} S_{31}^{\mathrm{B}} \beta \quad S_{24} = S_{23}^{\mathrm{A}} S_{32}^{\mathrm{B}} \beta \\ S_{31} &= S_{13}^{\mathrm{B}} S_{31}^{\mathrm{A}} \beta \quad S_{32} = S_{13}^{\mathrm{B}} S_{32}^{\mathrm{A}} \beta \\ S_{33} &= S_{11}^{\mathrm{B}} + S_{13}^{\mathrm{B}} S_{31}^{\mathrm{B}} \gamma \quad S_{34} = S_{12}^{\mathrm{B}} + S_{13}^{\mathrm{B}} S_{32}^{\mathrm{B}} \gamma \\ S_{41} &= S_{23}^{\mathrm{B}} S_{31}^{\mathrm{A}} \beta \quad S_{42} = S_{23}^{\mathrm{B}} S_{32}^{\mathrm{A}} \beta \\ S_{43} &= S_{21}^{\mathrm{B}} + S_{23}^{\mathrm{B}} S_{31}^{\mathrm{B}} \gamma \quad S_{44} = S_{22}^{\mathrm{B}} + S_{23}^{\mathrm{B}} S_{32}^{\mathrm{B}} \gamma \end{aligned}$$

where the values of multiplication parameters α, β, and γ are given in the following:

$$\alpha = \frac{\left(1 - S_{22}^{\mathrm{A\text{-}B}} S_{33}^{\mathrm{B}}\right) S_{11}^{\mathrm{A\text{-}B}} + S_{12}^{\mathrm{A\text{-}B}} S_{33}^{\mathrm{B}} S_{21}^{\mathrm{A\text{-}B}}}{\Delta}$$

$$\beta = \frac{S_{12}^{\mathrm{A\text{-}B}}}{\Delta}$$

$$\gamma = \frac{\left(1 - S_{11}^{\mathrm{A\text{-}B}} S_{33}^{\mathrm{A}}\right) S_{22}^{\mathrm{A\text{-}B}} + S_{12}^{\mathrm{A\text{-}B}} S_{33}^{\mathrm{A}} S_{21}^{\mathrm{A\text{-}B}}}{\Delta}.$$

Finally the denominator Δ yields

$$\Delta = \left(1 - S_{11}^{\mathrm{A\text{-}B}} S_{33}^{\mathrm{A}}\right)\left(1 - S_{22}^{\mathrm{A\text{-}B}} S_{33}^{\mathrm{B}}\right) - S_{12}^{\mathrm{A\text{-}B}} S_{21}^{\mathrm{A\text{-}B}} S_{33}^{\mathrm{A}} S_{33}^{\mathrm{B}}.$$

ACKNOWLEDGMENT

The authors would like to thank A. Mortara for the interesting insights and discussions and for carefully reading the article. They are also grateful to J. Hoffmann for valuable advice on simulations approach, to Jürg Rüfenacht for performing the VNA measurements and to Stefan Russi for the support in the mechanical design phase.

REFERENCES

[1] F. Overney and B. Jeanneret, "Impedance bridges: From wheatstone to Josephson," *Metrologia*, vol. 55, no. 5, pp. S119–S134, Oct. 2018.

[2] M. Zeier, J. Hoffmann, J. Ruefenacht, and M. Wollensack, "Contemporary evaluation of measurement uncertainties in vector network analysis," *Technisches Messen*, vol. 84, pp. 348–358, May 2017.

[3] L. Callegaro, "The metrology of electrical impedance at high frequency: A review," *Meas. Sci. Technol.*, vol. 20, Feb. 2009, Art. no. 022002.

[4] F. A. Ziade, A. Morilhat, A. Bounouh, A. Poletaeff, C. Serrano, and D. Allal, "Traçabilité des mesures daimpédance electrique entre 100 kHz et 10 MHz," *Revue Française de Métrologie*, vol. 30, pp. 3–11, Feb. 2013.

[5] S. A. Awan and B. P. Kibble, "Towards accurate measurement of the frequency dependence of capacitance and resistance standards up to 10 MHz," *IEEE Trans. Instrum. Meas.*, vol. 54, no. 2, pp. 516–520, Apr. 2005.

[6] A. S. Awan and P. B. Kibble, "A universal geometry for calculable frequency-response coefficient of LCR standards and new 10-MHz resistance and 1.6-MHz quadrature-bridge systems," *IEEE Trans. Instrum. Meas.*, vol. 56, no. 2, pp. 221–225, Apr. 2007.

[7] H. J. Kim, R. D. Lee, and Y. P. Semenov, "Resistors with calculable frequency dependencies up to 1 MHz," *IEEE Trans. Instrum. Meas.*, vol. 56, no. 2, pp. 453–457, Apr. 2007.

[8] L. Vojačková, J. Kučera, J. Hromadka, and J. Boháček, "Calculation of high frequency 4-TP impedance standards," in *Proc. Conf. Precis. Electromagn. Meas. (CPEM)*, Jul. 2016, pp. 1–2.

[9] S. Maslan, J. Horska, M. Sira, and T. Skalicka, "Bridging the LF-RF gap for calibration of the RLC meters," in *Proc. Conf. Precis. Electromagn. Meas. (CPEM)*, Jul. 2018, pp. 1–2.

[10] P. Y. Semenov and A. O. Shvedov, "Multifilar resistors from DC up to 30 MHz," in *Proc. Conf. Precis. Electromagn. Meas. (CPEM)*, Jul. 2018, pp. 1–2.

[11] F. Ziade, A. Poletaeff, and D. Allal, "Primary standard for S-parameter measurements at intermediate frequencies (IFs)," *IEEE Trans. Instrum. Meas.*, vol. 62, no. 3, pp. 659–666, Mar. 2013.

[12] F. Mubarak, E. Dierikx, and G. Rietveld, "Traceable DC-18 GHz characterization of coaxial 50 Ω impedance standards," in *Proc. Conf. Precis. Electromagn. Meas. (CPEM)*, Jul. 2016, pp. 1–2.

[13] K. Suzuki, "A new universal calibration method for four-terminal-pair admittance standards," *IEEE Trans. Instrum. Meas.*, vol. 40, no. 2, pp. 420–422, Feb. 1991.

[14] L. Callegaro and F. Durbiano, "Four-terminal-pair impedances and scattering parameters," *Meas. Sci. Technol.*, vol. 14, no. 4, pp. 523–529, Apr. 2003.
[15] T. Özkan, G. Gülmez, Y. Gülmez, E. Turhan, and N. B. Teşneli, "Uncertainty analysis of four-terminal-pair capacitance characterization up 30 MHz," *MAPAN*, vol. 28, no. 2, pp. 85–90, Jun. 2013.
[16] S. Singh, S. Kumar, and T. John, "Realization of four-terminal-pair capacitors as reference standards of impedance at high frequency using impedance-matrix method," *IEEE Trans. Instrum. Meas.*, vol. 66, no. 8, pp. 2129–2135, Aug. 2017.
[17] M. Agustoni and F. Overney, "Impedance metrology: Bridging the LFRF gap," *IEEE Trans. Instrum. Meas.*, vol. 70, pp. 1–8, 2021.
[18] R. J. Haddad, "A Resistor Calculable from DC to $\omega = 10^5\ rad/s$," Ph.D. thesis, Fac. Shool Eng. Appl. Sci., George Washington Univ., Washington, DC, USA, 1969.
[19] *COMSOL Multiphysics V. 6.0*, COMSOL AB, Stockholm, Sweden. Accessed: Sep. 2022. [Online]. Available: www.comsol.com
[20] R. D. Cutkosky, "Four-terminal-pair networks as precision admittance and impedance standards," *IEEE Trans. Commun. Electron.*, vol. CE-83, no. 70, pp. 19–22, Jan. 1964.
[21] D. M. D. Pozar, *Microwave Engineering*. Hoboken, NJ, USA: Wiley, 2012.
[22] P. L. D. Peres, C. R. de Souza, and I. S. Bonatti, "ABCD matrix: A unique tool for linear two-wire transmission line modelling," *Int. J. Electr. Eng. Educ.*, vol. 40, no. 3, pp. 220–229, Jul. 2003.
[23] L. Wedepohl and D. Wilcox, "Transient analysis of underground power-transmission systems. System-model and wave-propagation characteristics," *Proc. Inst. Elect. Eng.*, vol. 120, no. 2, pp. 253–260, 1973.
[24] S. A. Schelkunoff, "The electromagnetic theory of coaxial transmission lines and cylindrical shields," *Bell Syst. Tech. J.*, vol. 13, no. 4, pp. 532–579, Oct. 1934.
[25] D. A. Frickey, "Conversions between S, Z, Y, H, ABCD, and T parameters which are valid for complex source and load impedances," *Trans. Microw. Theory Techn.*, vol. 42, no. 2, pp. 205–211, Feb. 1994.
[26] M. Zeier, J. Hoffmann, and M. Wollensack, "*Metas.UncLib*—A measurement uncertainty calculator for advanced problems," *Metrologia*, vol. 49, pp. 809–815, Dec. 2012.
[27] J. Boh Cek, "EUROMET project 432: Frequency performance of 12 906 and 6453 reference resistors for AC quantum Hall effect experiments," *Metrologia*, vol. 39, no. 2, pp. 231–237, Apr. 2002.

Marco Agustoni (Member, IEEE) was born in Mendrisio, Switzerland, in 1984. He received the M.S. degree in physics from the Swiss Federal Institute of Technology, Zurich, Switzerland, in 2008, and the Ph.D. degree in particle physics from the University of Bern, Switzerland, in 2013. He participated in the ATLAS Experiment at CERN, Geneva, Switzerland. In 2014, he joined the Federal Institute of Metrology, Bern-Wabern, Switzerland. His current research interests include signal processing and network communication systems, as well as design of new impedance standards bridging the low frequency–radio frequeny (LF–RF) gap.

Sophie De Préville was born in El Salvador, in 1992. She received the M.S. degree in microengineering from the University of Applied Sciences HES-SO, Lausanne, Switzerland, in 2020.

After a master thesis on the study of the mixed-mode S parameters in the field of connectors, she joined the Federal Institute of Metrology, Bern-Wabern, Switzerland. Her present work, in the High Frequency Laboratory, is focused on the development and characterization of measurement systems, particularly through the use of numerical simulation.

Frédéric Overney (Member, IEEE) was born in Yverdon, Switzerland, in 1967. He received the M.S. degree in physics from the Swiss Federal Institute of Technology, Lausanne, Switzerland, in 1995. He then joined the Federal Institute of Metrology METAS, Bern-Wabern, Switzerland, where he extended the measurement capabilities in the field of the ac/dc transfer up to 1000 V, participated in the evaluation, modification and characterization of atomic clock comparison system based on GPS signals. He has also been involved in the development of transformers-based coaxial ac-bridges for studying the ac quantum Hall effect. His present work is focused on the development of new measuring systems for impedance metrology, sampling bridges, digitally assisted bridges and dual Josephson impedance bridges. He is also working on the design of new impedance standards with calculable frequency dependence over a broad frequency range, bridging the low frequency–radio frequeny (LF–RF) gap.